Journal of Physics:
Conference Series

PURPOSE-LED PUBLISHING™

PAPER • OPEN ACCESS

Pyrolysis of biomass in fluidized-bed reactors: towards a data-driven approach for reactor design and control

To cite this article: Matteo Baldelli *et al* 2025 *J. Phys.: Conf. Ser.* **3143** 012010

View the article online for updates and enhancements.

You may also like

- Fluidized Bed Reactors for energy recovery from biomass and wastes: a data-driven approach towards the development of digital twins for real time control and monitoring
Matteo Baldelli, Lorenzo Bartolucci, Stefano Cordiner et al.
- Analysis of Deep Learning Methods for Modelling Levelized Cost of Hydrogen Generation from Solar/Wind Hybrid Systems at Various Locations in Oman
Satyanarayana Bora, Joseph Sekhar Santhappan and Lakshmana Rao Kalabarige
- Predicting biogas production in real scale anaerobic digester under dynamic conditions with machine learning approach
M. Erdem Isenkul, Sevgi Güne-Durak, Yasemin Poyraz Kocak et al.

Enabling Electrochemistry Inside and Outside the Lab

PalmSens

Discover our diverse range of Potentiostats engineered to support your research wherever it takes you

- Intuitive software for Windows and Android
- Proven in over 4000 scientific publications
- Single-channel and multi-channel
- Benchtop, portable and wearable

Discover More



This content was downloaded from IP address 160.80.104.89 on 16/11/2026 at 14:14

Pyrolysis of biomass in fluidized-bed reactors: towards a data-driven approach for reactor design and control

Matteo Baldelli[1*], Lorenzo Bartolucci[1], Stefano Cordiner[1], and Vincenzo Mulone[1]

[1] Department of Industrial Engineering, Tor Vergata University of Rome, via del Politecnico 1, 00133, Rome, Italy

[*]E-mail: matteo.baldelli@uniroma2.it

Abstract. Pyrolysis of residual lignocellulosic biomass plays a crucial role in mitigating climate change by providing a sustainable pathway for carbon-neutral energy production. In particular, fast pyrolysis on fluidized-bed reactors is a promising route to renewable bio-oil and syngas, yet reactor design is complicated by the multiphase hydrodynamics and tight temperature-time windows needed to maximize liquid yields. A second key aspect for pyrolysis reactors is the flexibility. The performance of such systems is highly dependent on the composition of the feedstock, which strongly influences both the distribution and quality of the resulting products. Conventional design techniques rely on both empirical correlations and CFD models, which are computationally expensive and sensitive to uncertain feedstock properties. Recent advances in Machine Learning provide a data-driven alternative that can map complex, nonlinear relationships between operating variables and performance, with a time-scale of several orders of magnitude smaller than standard methods, enabling fast design procedures and reactor real-time control. In this work, the data from an extensive computational fluid dynamics (CFD) campaign on pyrolysis of lignocellulosic biomass in fluidized-bed reactors are used to train two Neural Networks (NNs): one aimed at predicting the composition of pyrolysis products (suitable for control application), and the other at providing reactor design guidelines based on the desired product output. The NNs test results indicate that the average prediction error is below 5 % relative to the actual target value, demonstrating the robustness of the models over the entire data-set.

1. Introduction

Energy and matter recovery from waste streams and residual biomasses plays a crucial role in the climate change mitigation and the resource scarcity challenge. Among all the possible processes that can be exploited to overcome the waste management and bio-fuel production problems, pyrolysis of lignocellulosic biomass has received particular attention due to the possibility of producing high-added-value products [1], [2], [3] Despite the intense research efforts of the scientific community, several challenges in the pyrolysis-based applications still remain open or not completely fulfilled[4], [5], [6].

Content from this work may be used under the terms of the Creative Commons Attribution 4.0 licence. Any further distribution of this work must maintain attribution to the author(s) and the title of the work, journal citation and DOI.
Published under licence by IOP Publishing Ltd

Pyrolysis is a thermo-chemical process conducted in inert atmosphere, in which a complex matrix is degraded into a large number of simpler compounds usually classified into three macro-categories: volatile vapor (gas), condensable vapor (oil) and solids (char) [7]. The biomass, first shredded to obtain small particles, is fed into a reactor which has, in general, two main tasks: maintaining an inert atmosphere, ensuring an efficient heat transfer, and thermal insulation. The inert atmosphere is usually maintained by continuously flowing a carrier gas (*e.g.* nitrogen) through the reactor, which also has the objective of controlling the residence time of the produced vapours within the reactor. The heat transfer is a fundamental aspect of pyrolysis application. The way the heat is supplied, the maximum temperature (pyrolysis temperature), the rate of temperature rise (heating rate), and the residence time, all strongly affect the final yield distribution of gas, oil, and char [1], [8], [9]. Because of the wide variety of process parameters, and due to the different desirable outputs, numerous reactor designs have been developed during the last century to optimise different aspects of the pyrolysis process[10]. Nonetheless, existing reactor configurations are often rigid, designed to process a specific waste type and tailored to obtain a particular output. The design is further complicated by the complex fluid dynamics phenomena and reaction mechanisms that occur in these reactors, many of which are also not yet fully understood[11][12]. As a result, reactor design remains a challenging task, where extrapolating findings from a laboratory scale to an industrial-scale reactor is not sufficient. Therefore, the reactor development often proceeds through by costly trial and error, requiring expensive experimental setups and long development time [13], [14].

With the exponential increase in computer performance of the last decades, numerical and simulation approaches provided useful tools to assist in the reactor design. Numerical approaches provide a significant acceleration in the design process, however, the trial-and-error principle still survives, since no exact theoretical laws exist for the reactor scale-up [15], [16]. Moreover, even nowadays, high-fidelity 3D simulations are still computationally demanding and time-consuming, limiting the systematic exploration of different reactor configurations and sensitivity analyses[12], [17]. For all these reasons, reliable, simple, and faster numerical methods are needed to speed up the design process. Over the past decade, data-driven and machine-learning (ML) approaches have attracted considerable interest of the scientific community, because they provide a different methodology to develop reliable and faster (if compared with experiments and standard CFD simulations) reduced order models (ROMs) [12], [18], [19], [20], [21]. In recent years, ML methods have been successfully applied in different fields of physics and engineering, demonstrating their value in predicting and describing complex phenomena [22], [23], [24].

In this work, we proposed the use of Neural Networks (NNs) as a tool for the design and control of fast-pyrolysis reactors (high heating rate). Specifically, we have analysed the pyrolysis of a lignocellulosic biomass in a fluidized-bed reactor, through an intensive CFD simulation campaign varying different process parameters such as pyrolysis temperature, reactor size, and gas carrier velocity. The data extracted from these CFD simulations, are used to train and test two different NNs, with distinct objectives. The Product Yield Net (PYN) predicts the product distribution given the reactor size and operating conditions. The second NN, named Reactor Design Net (RDN), provides a starting point for the reactor design by predicting the size and process parameters required to achieve the desired product distribution. Details of the CFD setup, network architecture and training procedure are presented in the Methods section, while simulation results and analysis of NN performance are reported and discussed in the Results section.

2. Methods

In this study, we proposed a data-driven approach for obtaining a starting point for fluidized-bed reactor design for the pyrolysis of cellulosic biomass and for control applications. In particular, two different NNs are trained to accomplish two different goals: the first one, for control purposes, is predicting the products composition given information about the reactor design, in terms of height H, diameter D, and process parameters such as the pyrolysis temperature T_{pyro}, and the inlet fluidizing gas (nitrogen) velocity $\boldsymbol{u}_{in,N_2}$ (features); the second goal is providing reactor design characteristics (H and D) and process parameters given the desired product distribution. Training and testing phase are carried out using data extracted from a CFD simulation campaign in which all the process and reactor parameters are varied exploiting a statistical sampling. In fact, in order to ensure a wide exploration of the parameter space for the training of the NNs, the Latin Hypercube Sampling (LHS) techniques is used. Moreover, a statistical sampling increase the reliability of the NNs predictions, since avoid to obtain strong bias during the learning phase due to the limited exploration of the parameter space. In the following paragraph, a detailed explanation of the CFD simulations and the NNs set-ups are provided.

2.1 Fluidized-bed reactor simulation campaign

In the numerical simulations, the reactor is modeled as a 2D rectangular domain with a diameter D (in 3D sense) and a height H. The domain is then discretized with an uniform mesh, where each element is a square with a side length of 5×10^{-4} m. It is important to note that, since the reactor size varies within the numerical campaign, the number of mesh elements is not constant for each simulation, while their size remains unchanged. To solve the physics and chemistry of the entire process, a multiphase Euler-Euler approach is used. In this numerical method both solid and fluid materials are treated as interpenetrating and interacting fluids. Regarding the solid phase, it is considered as a granular phase with specific properties that can be defined for each sub-species of the phase. In our simulation, three main material phases are considered: the primary phase is the nitrogen, used as a fluidizing gas; the first secondary solid granular phase is the sand, used as bed material; the last secondary granular phase is the biomass (cellulose). The latter is also divided into several species that are consumed and/or produced during the pyrolysis process, according to the cellulose chemical reaction scheme proposed by Ranzi *et. al* [25] and following the classical Arrhenius kinetics.

The description of multiphase flow in the Euler-Euler framework is based on the concept of species volume fraction. This means that the conservation laws (mass, momentum, and energy) are satisfied by each phase individually, averaging the contribution of each species in term of mass fraction, weighting with respect to its volume fraction that is defined as follows

$$V_i = \int_V \alpha_i dV, \tag{1}$$

such that

$$\sum_{i=1}^{n} \alpha_i = 1, \tag{2}$$

where V_i is the volume occupied by the ith species, V is the integration volume, α is the volume fraction, and n is the number of phases. The volume fraction of the ith phase, is therefore calculated from the continuity equation

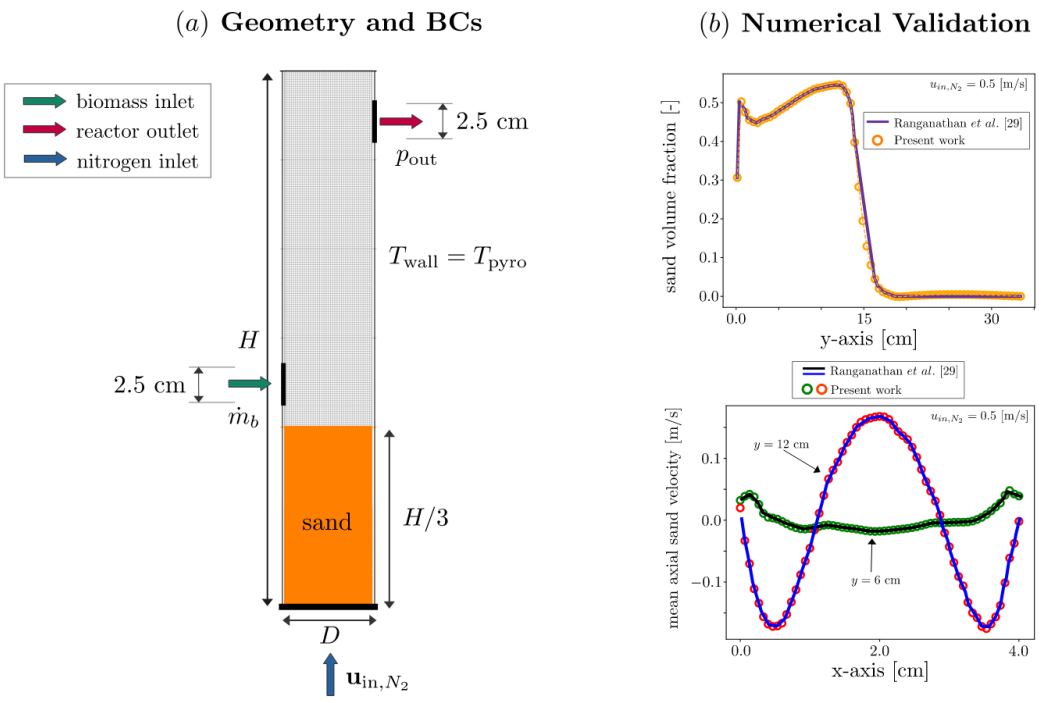


Figure 1: **CFD simulation set-up. (a)** Sketch of the reactor geometry (not in scale) with the numerical boundary conditions. In the simulation campaign, the reactor geometry is varied by modifying the height H and the diameter D. The sand (orange rectangle) is initialized to occupy 1/3 of the reactor volume (in 2D sense). The biomass inlet (green arrow) is positioned 2.0 cm above the sand bed, and has a diameter of 2.5 cm. At the bottom of the reactor, the nitrogen inlet (blue arrow) is placed, while the outlet is located on the upper part of the left reactor wall (red arrow), 5.0 cm below the top wall, with a diameter of 2.5 cm. **(b)** The mathematical model is validated comparing our trend of the sand volume fraction and the mean axial velocity with the one obtained by Ranganathan *et al.* [12] . Panel (b) is adapted from [22].

$$\frac{1}{\rho_{ri}}\left(\frac{\partial}{\partial\, t}(\alpha_i\rho_i) + \nabla\cdot(\alpha_i\rho_i\boldsymbol{u}_i) = \sum_{j=1}^{n}(\dot{m}_{ji} - \dot{m}_{ij})\right), \tag{3}$$

where ρ_{ri} is the reference density of the ith phase, t is the time, ρ is the local density of the specific phase, $\boldsymbol{u}$ is the velocity, and $\dot{m}_{ji}$ and $\dot{m}_{ij}$ are the transferred mass from phase j to phase i and vice versa, respectively. It is worth noting that Eq.(3) is solve only for the secondary phases (*i.e.* sand and biomass in our settings) and, together with Eq.(2), is used to calculate the volume fraction of the primary phase (*i.e.* nitrogen).

The conservation of momentum is formulated differently depending on whether the interaction occurs between two fluid phases or between fluid and solid phases. For fluid-fluid interaction and for the ith phase, the following equation for the momentum holds

$$\begin{aligned}\frac{\partial}{\partial t}(\alpha_i\rho_i\boldsymbol{u}_i) + \nabla\cdot(\alpha_i\rho_i\boldsymbol{u}_i\boldsymbol{u}_i) = \\ = -\,\alpha_i\nabla p + \nabla\cdot\boldsymbol{\tau} + \;\alpha_i\rho_i\boldsymbol{g}\; + \sum_{j=1}^{n}(K_{ij}(\boldsymbol{u}_j - \boldsymbol{u}_i) + \;\dot{m}_{ji}\boldsymbol{u}_{ji} - \dot{m}_{ij}\boldsymbol{u}_{ij}) + \boldsymbol{F}\;,\end{aligned} \tag{4}$$

where, p is the pressure $\boldsymbol{\tau}$ is the stress-strain tensor, $\boldsymbol{g}$ is gravitational the acceleration, K_{ij} is the interphase momentum exchange coefficient , $\boldsymbol{u}_{ij}$ and $\boldsymbol{u}_{ji}$ are the interphase velocities, whose value depends on the mass transfer between phases, and $\boldsymbol{F}$ is the force field that takes into account external body forces, lift forces and turbulent dispersion [26]. In a similar manner, the momentum conservation equation for fluid and solid phase interactions can be derived. Compared to Eq.(4), this formulation additionally includes the solid-phase pressure, which accounts for both kinetic aspects and particle collisions. For the granular temperature in the solid pressure formulation, the granular bulk viscosity and the granular viscosity are modelled using Lun *et. al* [27] and Syamlal *et. al* [28], [29] relationship, respectively.

Finally, the last conservation equation considered is the energy conservation, that is summarized for the sake of brevity as follows:

$$\frac{\partial}{\partial t}\left(\alpha_i \rho_i \left(e_i + \frac{\boldsymbol{u}_i^2}{2}\right)\right) = \nabla \cdot \dot{\boldsymbol{J}}_{is} + Q_{ij} + S_i \tag{5}$$

where, $\dot{\boldsymbol{J}}$ represents the heat flux of the ith phase, the energy of the species in that phase and the energy dissipation, Q_{ij} represents the interphase heat exchange [30],and S_i is a heat source term (*e. g.* due to chemical reactions). For a detailed discussion about the solved equations, the interested reader is referred to [31], [32].

Given the set of Eqs. (2)-((5) together with the species conservation equations, to close the numerical problem, a set of boundary conditions (BCs) should be provided. In the proposed set-up, the BCs are as follow: at the nitrogen inlet, placed at the reactor bottom, a constant velocity $\boldsymbol{u}_{in,N_2}$ and a constant temperature T_{pyro} are imposed; at the outlet (top right section of the reactor), a fixed pressure $p_{out} = 101325$ Pa is used; fixed temperature T_{pyro} and no-slip condition are imposed along the reactor walls; at the biomass inlet, a constant mass flow of $\dot{m}_b = 8.3 \times 10^{-5}$ kg/s is considered at environment temperature. See Fig. 1(a) for a graphical representation of the BCs. Finally, each simulation is initialized with a sand bed with a height of $H/3$ and a constant temperature T_{pyro}, within the reactor. The numerical setting is solved using the commercial software Ansys® and it is validated against the results obtained by Ranganathan *et. al* [12] and presented in Fig. 1(b).

As mentioned above, the simulation campaign is used to populate the dataset needed for training and testing the proposed NNs. To increase the reliability of the NN results, the dataset should be populated with data with a large variance, in order to increase the exploration of the parameter space. To do so, a LHS method is used varying the following parameters: reactor height H, reactor diameter D, pyrolysis temperature T_{pyro}, and the inlet gas velocity $\boldsymbol{u}_{in,N_2}$. In Table 1 the parameter ranges are summarized. Moreover, as a consequence of the parameter variation, other quantities are varied, in particular the sand height ($= H/3$), the position of the biomass inlet and the reactor outlet, see Figure 1(a) for details. This sampling method provides a total of 26 different simulations, corresponding to 26 distinct design points (DPs) in the parameter space, that are presented in the normalized 3D projections form of the 4D parameter space in Figure 2 ($(H, D, T_{\text{pyro}}, \boldsymbol{u}_{in,N2}) \in \mathbb{R}^4$).

Table 1. **Reactor parameter ranges**. In the table the parameters varied in the CFD simulation campaign, together with their symbols, range and unit measures, are reported.

Parameter	Symbol	Range	Unit
Height	H	$0.34 - 1.0$	m
Diameter	D	$0.04 - 0.15$	m
Pyrolysis temperature	T_{pyro}	$723 - 873$	K
N_2 velocity	$\boldsymbol{u}_{in,N_2}$	$0.03 - 1.0$	m/s

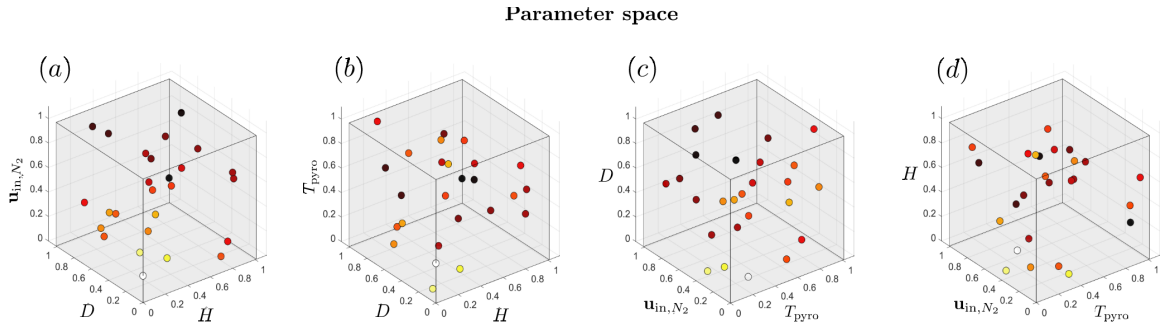


Figure 2. **Parameter space of the CFD campaign.** The panels summarized the design points for each simulation. In particular, they show the point distribution for all the combination of $(H, D, T_{\text{pyro}}, \boldsymbol{u}_{in,N2}) \in \mathbb{R}^4$. For graphical reason and for the sake of clarity, the parameters are normalized with respect to the minimum and maximum value. The actual range for each parameter is reported in Table 1.

2.2 Neural Networks design

In this study, we propose the use of two NNs, each tailored to a specific task. The first, called Product Yield Net (PYN), predicts pyrolysis products from the key operating parameters (features) T_{pyro}, $\boldsymbol{u}_{in,N_2}$, and the reactor size, H and D. The second one, hereafter referred to as the Reactor Design Net (RDN), provide reactor geometry, $\frac{H}{D}$, and the operating conditions, T_{pyro} and $\boldsymbol{u}_{in,N_2}$, that achieve the desired product distribution. Although, the two NNs have different objectives, they share the same core principle. The similarities, allow us to apply the same techniques to determine an appropriate architecture (*e.g.* number of hidden layers and neurons) and an effective training method.

The training phase begins with the assumption that the neural network architecture and all necessary hyperparameters for optimization have already been defined. Since there are no universally accepted theoretical rules for selecting these hyperparameters, whether architectural (*e.g.* number of layers and neurons) or related to the optimization process itself (*e.g.* learning rate, size of validation and test sets), an iterative algorithm was adopted for their determination. Specifically, the algorithm starts with an initial guess for the network architecture, defined by the number of layers (n_l), the number of neurons per layer (n_n), and a fixed number of training epochs (n_e). For each combination of (n_l, n_n, n_e), the algorithm evaluates the network's predictive performance using the root mean square error (RMSE) as a metric:

$$E_{\text{RMSE}} = \left(\sum_{k=1}^{m} \frac{(\hat{y}_k - y_k)^2}{m} \right)^{\frac{1}{2}}, \tag{6}$$

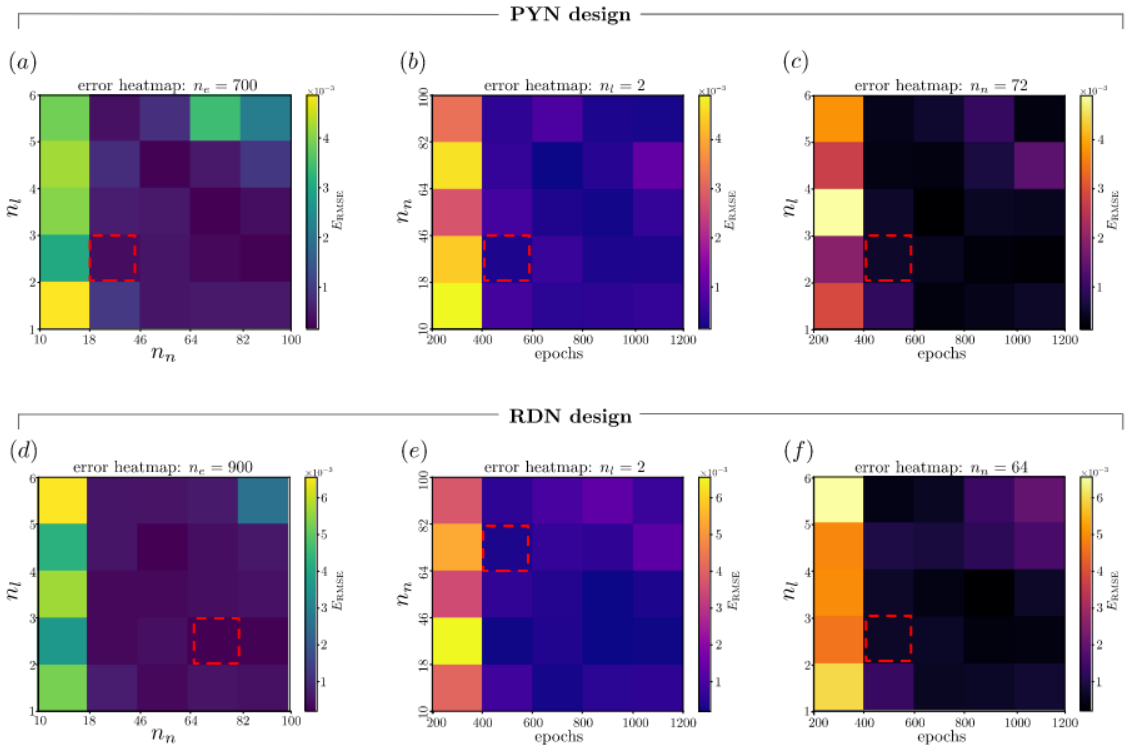


Figure 3. **NN design results**. Heatmaps of the loss function evaluated for the optimal value of (n_l, n_n, n_e). **(a-c)** Heatmaps of the E RMSE evaluated for the optimal value of (n_l, n_n, n_e) of PYN, obtained from the iterative design algorithm. **(d-f)** Heatmaps of the E_{RMSE} evaluated for the optimal value of (n_l, n_n, n_e) for the RDN, obtained by the iterative design algorithm. It is important to note that the values of each parameter are clustered with respect to the error they provide. The red dashed squares represent the optimal design points.

where m is the output size, y is the actual target, and $\hat{y}$ is the NN predictions. It then iteratively explores different combinations of (n_l, n_n, n_e) within predefined ranges to identify the set that minimizes the error. In particular, to reduce the probability of overfitting, the following constraints for the model hyperparameter are imposed: $n_l \leq 6$, $n_n \leq 100$, and $n_e \leq 10^4$. The itarative algorithm also requires prior definition of optimization hyperparameters, such as activation functions and training strategy. In this study, the dataset was split into 70% for training, 15% for validation, and 15% for testing. All input features and output targets are normalized between 0 and 1. This normalization is essential due to the varying magnitudes of the different features (*e.g.* temperature versus fluidizing gas velocity), which could otherwise lead to unbalanced weight updates during training. Regarding activation functions, sigmoid function is used in the hidden layers for both PYN and RDN, while a softmax function is applied at the output layer of the PYN, and a ReLU function is used in output layer of the RDN. The learning rate is kept constant $l_r = 0.001$ in each algorithm iteration. The resulting architectures for PYN and RDN networks are summarized in Table 2 and depicted in Figure 3.

Table 2. **Neural Network hyperparameters**. Model hyperparameters resulting from the optimization algorithm. In the first columns the names of the proposed NNs, are reported. In the second one, the number of hidden layers obtained from the algorithm can be found. While in the third and last columns, the number of neurons per layer and the epochs required for the training are reported, respectively.

Net name	Hidden layers (n_l)	Neurons (n_n)	Epochs (n_e)
PYN	2	24	430
RDN	2	72	570

3. Results

3.1 Fluidized-bed reactor simulation results

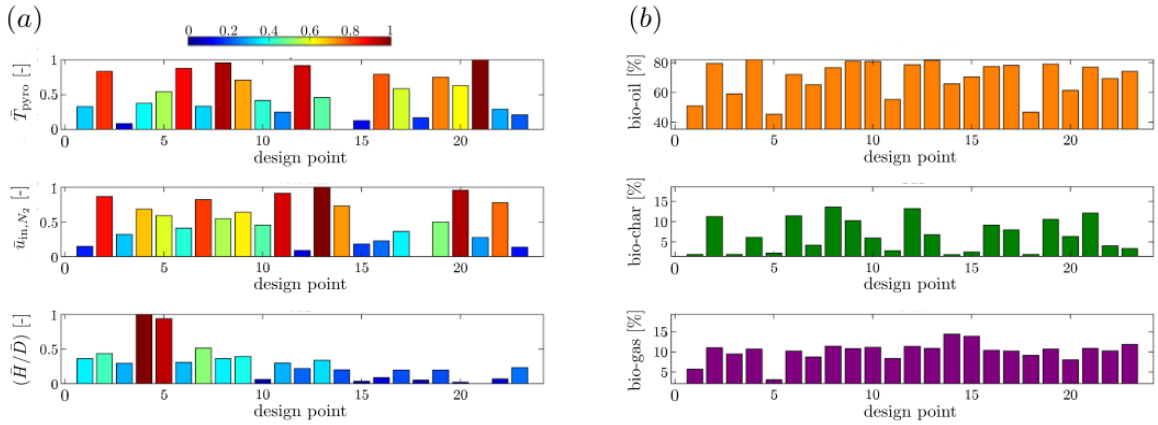


Figure 4. **CFD simulation results. (a)** Normalized parameters used in the CFD simulations campaign for each dp. **(b)** Product distribution for each DP. The orange bars represent the bio-oil, the green bars are the char distribution, and the violet ones describe the gas production.

In Figure 4, the effect of the different operating conditions on product distribution for the entire CFD simulation campaign, are summarized. Specifically, the Fig.4(a) condenses the three independent variables explored in the simulation campaign, all normalized to the range 0-1 and colour-coded to facilitate a visual comparison. The sampling strategy spans the full operating windows of practical interest in fast pyrolysis applications: low-severity cases with relatively mild temperatures and slow gas flow coexist with highly severe conditions characterised by elevated temperatures and fast hydrodynamics. The Fig. 4(b), shows the obtained mass fraction of bio-oil, bio-char and gas for each design point. Bio-oil, is the dominant product across all the simulations, consistently exceeding the 45 % and reaching as high as 82 %, confirming that all conditions lie within the fast-pyrolysis regime. Nevertheless, clear trends emerge when the three inputs are examined together. DPs combining high pyrolysis temperature and high superficial gas velocity (*e.g.* DPs 8, 12, and 19) exhibit the most pronounced secondary cracking, which provides the highest gas yields ($\simeq$ 16 %) and the lowest char production (< 5 %). In contrast, simulations performed at moderate temperatures but with pronounced aspect ratio (H/D > 0.6) favour incomplete devolatilization, so that char can exceed 10 % in weight while the gas flow drops

below 6 %. Intermediate settings produce a more balanced distribution, where the oil is around 80 % with a char between 5-8 % and gas between 8–12 %. Moreover, the results highlight how the same product distribution can be obtained with different operating parameters and reactor size. For example, the DP 4, characterized by a low pyrolysis temperature, a high $\boldsymbol{u}_{in,N_2}$ (small residence time), and a large H/D ratio, yields nearly the same bio-oil, char and gas fractions as the DP 16, which operates at a high temperature, slow carrier-gas flow (large residence time), and a small aspect ratio. The similarity between these opposite settings highlights the strong compensating interactions and interplay among the parameters analysed, and due to the highly non linearities that these parameters have on the pyrolysis process, is it clear that try to infer common behaviour for specific conditions and transfer this knowledge in a completely different situations is afflicted by uncertainties. The following section demonstrates how NN surrogate models, calibrated with an extended CFD data set, can capture these underlying effects and thereby provide a rapid, predictive framework for reactor design and control.

3.2 Neural Networks results

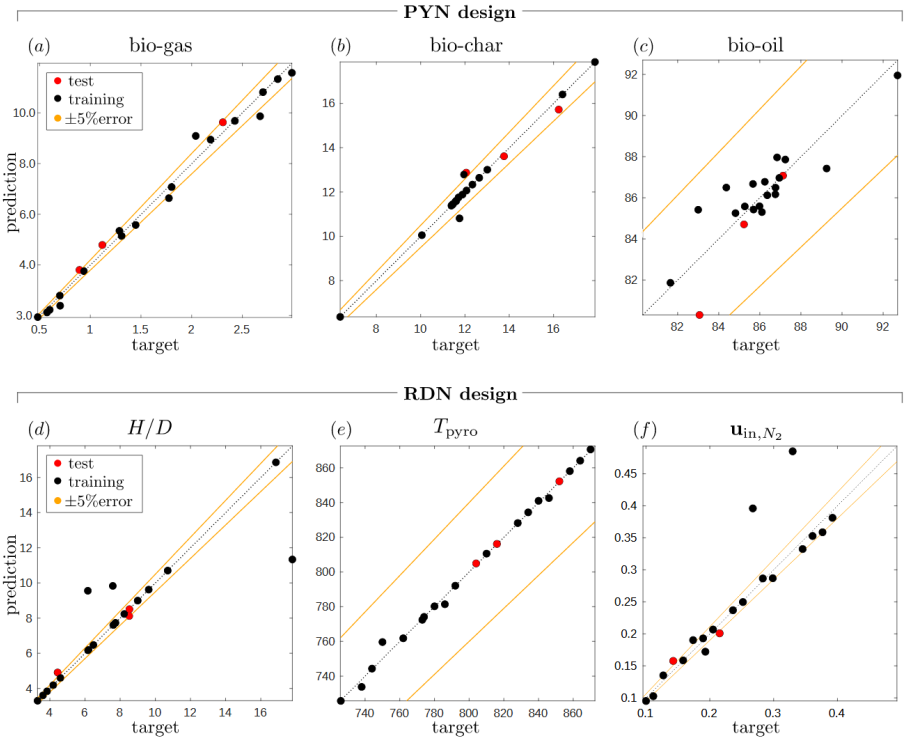


Figure 5. **PYN and RDN results. (a-c)** PYN prediction results for the three product categories. In panel (a) the performances of the NN on predicting the bio-oil production, are reported. In panels (b) and (c), prediction results of bio-char and gas yields are shown. **(d-f)** Results on design parameter predictions of the RDN network are reported. In all the panels the black dots and red dots represents the DP used for training and testing, respectively. The black dashed lines describe the perfect prediction, while the orange solid lines represent the 5 % error bounds.

As mentioned in the Methods section, the data gathered from the CFD simulation campaign are used to train the two NNs: PYN and RND. In Fig. 5, the comparison of NNs output with the reference CFD data for both the forward PYN and the inverse RDN, is reported.

In the upper row of Fig. 5, panels (a-c), the ability of PYN to reproduce the three product fractions is demonstrated. The PYN aims to predict the product distribution divided in the three macro-categories bio-oil, bio-char, and bio-gas, therefore is suited for control purposes. The prediction is performed using as input features the reactor geometry (aspect ratio) and the process operating conditions: $(H/D, T_{\mathrm{pyro}}, \boldsymbol{u}_{\mathrm{in},N_2})$. Predictions for bio-oil and bio-char cluster tightly along the quadrant bisector line (perfect prediction) and most points fall inside the 5 % error bounds, indicating that the network has learned the dominant, monotonic dependence of these two phases on temperature, gas carrier velocity (residence time) and geometry. Bio-gas shows a slightly larger scatter, particularly for targets near the lower end of the explored range, yet even in this case more than 90 % of the samples remain within the predefined tolerance. Moreover, the increased dispersion is consistent with the narrower dynamic span of the gas fraction, which amplifies the impact of any absolute deviation when plotted on percentage axes.

In the bottom row of Fig. 5, panels (d-f), the performance of the RDN, which must invert the highly non-linear mapping and infer reactor settings from a prescribed product distribution, is presented. Panel (d) shows that the aspect ratio H/D is predicted with high fidelity over the entire interval explored. The larger dispersions are due to the complicated relationship between the aspect ratio and the nitrogen velocity. In fact, as highlighted in the previous section, different combinations of the pairs $(H/D, \boldsymbol{u}_{\mathrm{in},N_2})$ can provide the same product fractions, since both of them are related to the heating rate and residence time in opposite way.

Fig. 5(e) shows that the network reproduces the target pyrolysis temperature almost exactly. This high accuracy is unsurprising and expected, because temperature exerts a well-defined, monotonic influence on product distribution: low temperatures favour char formation; intermediate temperatures maximise bio-oil yield; and high temperatures promote secondary cracking, consequently increasing the gas fraction at the expense of the other products. Carrier-gas velocity, Fig. 5(f), is one of the most challenging variables together with the aspect ratio, because it simultaneously controls hydrodynamics and vapour residence time; nonetheless, only two train points stray outside the ±5 % error bound. Despite the complicated interaction between the three design variables, the RDN performances confirm that the network has captured the compensating interactions among temperature, geometry and superficial velocity that were highlighted in the previous section, thereby enabling a reliable inverse design capability.

Taken together, the parity plots establish that both surrogate models generalise beyond their training samples and can predict unseen operating points with engineering accuracy. This level of agreement validates the use of the PYN–RDN pair as a rapid, data-driven substitute for iterative CFD calculations in preliminary design and real-time optimisation of fluidised-bed pyrolysers.

Conclusions

Scale-up, design, and control procedures are challenging aspects in pyrolysis applications, usually requiring a trial-and-error loops to be accomplished. Experimental campaign and high-fidelity CFD simulations, require both expensive apparatus and long period of time for studying different reactor configurations. Reduced-order models (ROMs), offer a promising alternative, providing solutions in computational times that are several orders of magnitude shorter that full CFD and experiments. Even when a ROM does not propose an immediately optimal design, it could provide a reliable starting point that can be refined with conventional high-fidelity approaches.

In this study, we have employed neural networks (NNs) as ROMs for fluidized-bed reactor design and control applications. An extensive CFD campaign, comprising 26 simulations

generated through Latin hypercube sampling method, is carried out to build the data-set needed for NNs training and testing processes. Each simulation features a unique combination of the reactor aspect ratio H/D, pyrolysis temperature T_{pyro}, and inlet nitrogen superficial velocity $\boldsymbol{u}_{\mathrm{in},N_2}$. The CFD results confirm that bio-oil remains the dominant product in (45-82 %) in the fast pyrolysis regime, while gas and char yields respond with high non-linearities to the coupled effects of H/D and $\boldsymbol{u}_{\mathrm{in},N_2}$. High-severity conditions maximize secondary cracking and gas formation, whereas tall reactors, at moderate temperatures, favor char production. Moreover, different combinations of the operating variables can yield similar product distribution, illustrating compensating interactions.

The resulting data are used to calibrate two distinct networks. The Product Yield Net (PYN) predicts the char, oil, and gas fractions given $\left(H/D, T_{\mathrm{pyro}}, \boldsymbol{u}_{\mathrm{in},N_2}\right)$ as a input features. The Reactor Design Network (RDN) is trained to solve the inverse problem, returning the operating triplet $\left(H/D, T_{\mathrm{pyro}}, \boldsymbol{u}_{\mathrm{in},N_2}\right)$ required to achieve the specified product distribution. Performances are assessed via prediction error (*i.e.* root mean square error), and both networks achieve mean absolute error below 5 %, confirming their accuracy, reliability and suitability for fast, data-driven design and control tools of pyrolysis in fluidized-bed reactors.

Acknowledgements

The authors acknowledge support from Project ECS 0000024 Rome Technopole- CUP: E83C22003240001, NRP Mission 4 Component 2 Investment 1.5, Funded by the European UnionNextGenerationEU.

References

[1] T. Kan, V. Strezov, and T. J. Evans, "Lignocellulosic biomass pyrolysis: A review of product properties and effects of pyrolysis parameters," *Renewable and sustainable energy reviews*, vol. 57, pp. 1126–1140, 2016.
[2] G. Wang *et al.*, "A review of recent advances in biomass pyrolysis," *Energy & fuels*, vol. 34, no. 12, pp. 15557–15578, 2020.
[3] M. Baldelli, L. Bartolucci, S. Cordiner, E. De Maina, and V. Mulone, "Toward carbon neutral fuels: Process analysis of integrated biomass conversion routes for sustainable biofuels production," *Energy*, vol. 324, p. 136077, 2025.
[4] G. R. Mong *et al.*, "Progress and challenges in sustainable pyrolysis technology: Reactors, feedstocks and products," *Fuel*, vol. 324, p. 124777, 2022.
[5] G. Yildiz, F. Ronsse, R. Van Duren, and W. Prins, "Challenges in the design and operation of processes for catalytic fast pyrolysis of woody biomass," *Renewable and Sustainable Energy Reviews*, vol. 57, pp. 1596–1610, 2016.
[6] M. Rüdisüli, T. J. Schildhauer, S. M. A. Biollaz, and J. R. Van Ommen, "Scale-up of bubbling fluidized bed reactors—A review," *Powder Technol*, vol. 217, pp. 21–38, 2012.
[7] L. Bartolucci, S. Cordiner, A. Di Carlo, A. Gallifuoco, P. Mele, and V. Mulone, "Platform chemicals recovery from spent coffee grounds aqueous-phase pyrolysis oil," *Renew Energy*, vol. 220, p. 119630, 2024.
[8] A. A. Papa *et al.*, "The effect of pyrolysis temperature on the optimal conversion of residual biomass to clean syngas through fast-pyrolysis/steam gasification integration," *Int J Hydrogen Energy*, vol. 95, pp. 1316–1327, 2024.
[9] D. Sorino *et al.*, "Pyrolysis of mixed contaminated plastic wastes: Assessing the influence of polymers composition, temperature and residence time," *Waste Management*, vol. 201, p. 114793, 2025.
[10] J. W. Chew, W. C. Q. LaMarche, and R. A. Cocco, "100 years of scaling up fluidized bed and circulating fluidized bed reactors," *Powder Technol*, vol. 409, p. 117813, 2022.
[11] P. Mellin, Q. Zhang, E. Kantarelis, and W. Yang, "An Euler-Euler approach to modeling biomass fast pyrolysis in fluidized-bed reactors - Focusing on the gas phase," *Appl Therm Eng*, vol. 58, no. 1–2, pp. 344–353, 2013, doi: 10.1016/j.applthermaleng.2013.04.054.

[12] P. Ranganathan and S. Gu, "Computational fluid dynamics modelling of biomass fast pyrolysis in fluidised bed reactors, focusing different kinetic schemes," *Bioresour Technol*, vol. 213, pp. 333–341, Aug. 2016, doi: 10.1016/j.biortech.2016.02.042.
[13] T. M. Knowlton, "Fluidized bed reactor design and scale-up," in *Fluidized bed technologies for near-zero emission combustion and gasification*, Elsevier, 2013, pp. 481–523.
[14] T. M. Knowlton, S. B. R. Karri, and A. Issangya, "Scale-up of fluidized-bed hydrodynamics," *Powder Technol*, vol. 150, no. 2, pp. 72–77, 2005.
[15] N. Couto, V. B. Silva, C. Bispo, and A. Rouboa, "From laboratorial to pilot fluidized bed reactors: Analysis of the scale-up phenomenon," *Energy Convers Manag*, vol. 119, pp. 177–186, 2016.
[16] J. M. Matsen, "Scale-up of fluidized bed processes: Principle and practice," *Powder Technol*, vol. 88, no. 3, pp. 237–244, 1996.
[17] S. R. A. Kersten, X. Wang, W. Prins, and W. P. M. Van Swaaij, "Biomass pyrolysis in a fluidized bed reactor. Part 1: Literature review and model simulations," Nov. 09, 2005. doi: 10.1021/ie0504856.
[18] L. T. Zhu *et al.*, "Review of Machine Learning for Hydrodynamics, Transport, and Reactions in Multiphase Flows and Reactors," Jul. 20, 2022, *American Chemical Society*. doi: 10.1021/acs.iecr.2c01036.
[19] S. L. Brunton, J. L. Proctor, and J. N. Kutz, "Discovering governing equations from data by sparse identification of nonlinear dynamical systems," *Proc Natl Acad Sci U S A*, vol. 113, no. 15, pp. 3932–3937, 2016, doi: 10.1073/pnas.1517384113.
[20] P. Dubois, T. Gomez, L. Planckaert, and L. Perret, "Machine learning for fluid flow reconstruction from limited measurements," *J Comput Phys*, vol. 448, Jan. 2022, doi: 10.1016/j.jcp.2021.110733.
[21] S. Walton, O. Hassan, and K. Morgan, "Reduced order modelling for unsteady fluid flow using proper orthogonal decomposition and radial basis functions," *Appl Math Model*, vol. 37, no. 20–21, pp. 8930–8945, Nov. 2013, doi: 10.1016/j.apm.2013.04.025.
[22] M. Baldelli, L. Bartolucci, S. Cordiner, and V. Mulone, "Fluidized Bed Reactors for energy recovery from biomass and wastes: a data-driven approach towards the development of digital twins for real time control and monitoring," in *Journal of Physics: Conference Series*, IOP Publishing, 2024, p. 012014.
[23] V. Krastev, M. Baldelli, L. Bartolucci, G. Falcucci, V. Mulone, and S. Cordiner, "Towards the adoption of neural-network-based solvers for coupled mh-pcm hydrogen storage devices," in *ECOS 2024*, 2024, pp. 776–787.
[24] S. L. Brunton, B. R. Noack, and P. Koumoutsakos, "Machine learning for fluid mechanics," *Annu Rev Fluid Mech*, vol. 52, no. 1, pp. 477–508, 2020.
[25] E. Ranzi *et al.*, "Chemical kinetics of biomass pyrolysis," *Energy & Fuels*, vol. 22, no. 6, pp. 4292–4300, 2008.
[26] D. Gidaspow, R. Bezburuah, and J. Ding, "Hydrodynamics of circulating fluidized beds: kinetic theory approach," Illinois Inst. of Tech., Chicago, IL (United States). Dept. of Chemical …, 1991.
[27] C. K. K. Lun, S. B. Savage, D. J. Jeffrey, and N. Chepurniy, "Kinetic theories for granular flow: inelastic particles in Couette flow and slightly inelastic particles in a general flowfield," *J Fluid Mech*, vol. 140, pp. 223–256, 1984.
[28] M. Syamlal, "The particle-particle drag term in a multiparticle model of fluidization," EG and G Washington Analytical Services Center, Inc., Morgantown, WV (USA), 1987.
[29] M. Syamlal and T. J. O'Brien, "The derivation of a drag coefficient formula from velocity-voidage correlations," *Technical Note, US Department of energy, Office of Fossil Energy, NETL, Morgantown, WV*, 1987.
[30] D. J. Gunn, "Transfer of heat or mass to particles in fixed and fluidised beds," *Int J Heat Mass Transf*, vol. 21, no. 4, pp. 467–476, 1978.
[31] "Ansys Fluent Theory Guide," 2024. [Online]. Available: http://www.ansys.com
[32] "Ansys Fluent User's Guide," 2024. [Online]. Available: http://www.ansys.com